Available online at www.sciencedirect.com
SCIENCE DIRECT®
Journal of Magnetic Resonance 164 (2003) 242–255
JMR Journal of Magnetic Resonance
www.elsevier.com/locate/jmr

Planar microcoil-based microfluidic NMR probes

C. Massin,[a,*] F. Vincent,[a] A. Homsy,[b] K. Ehrmann,[a] G. Boero,[a] P.-A. Besse,[a] A. Daridon,[b,1] E. Verpoorte,[b] N.F. de Rooij,[b] and R.S. Popovic[a]

[a] *Institute of Microelectronics and Microsystems, EPFL—Swiss Federal Institute of Technology Lausanne, BM 3.108, Lausanne CH-1015, Switzerland*
[b] *SAMLAB, Institute of Microtechnology, University of Neuchâtel, Switzerland*

Received 11 March 2003; revised 14 April 2003

Abstract

Microfabricated small-volume NMR probes consisting of electroplated planar microcoils integrated on a glass substrate with etched microfluidic channels are fabricated and tested. ^{1}H NMR spectra are acquired at 300 MHz with three different probes having observed sample volumes of respectively 30, 120, and 470 nL. The achieved sensitivity enables acquisition of an ^{1}H spectrum of 160 μg sucrose in D_2O, corresponding to a proof-of-concept for on-chip NMR spectroscopy. Increase of mass-sensitivity with coil diameter reduction is demonstrated experimentally for planar microcoils. Models that enable quantitative prediction of the signal-to-noise ratio and of the influence of microfluidic channel geometry on spectral resolution are presented and successfully compared to the experimental data. The main factor presently limiting sensitivity for high-resolution applications is identified as being probe-induced static magnetic field distortions. Finally, based on the presented model and measured data, future performance of planar microcoil-based microfluidic NMR probes is extrapolated and discussed.

Keywords: Small-volume NMR; Microcoils; μTAS; Microfluidics; Signal-to-noise ratio; Limits of detection; Spectral resolution

1. Introduction

The miniaturization of NMR detection coils aims at achieving increased sensitivity for analysis of mass-limited samples. The design and performance of solenoid radio-frequency (RF) coils with dimensions below 1 mm and active volume as low as 5 nL has been investigated in detail [1–4]. An improvement in mass-sensitivity of more than two orders of magnitude compared to conventional 5-mm NMR probes has been experimentally demonstrated [5]. Spatially localized NMR spectra of metabolites from single isolated neurons have been obtained [6], and the feasibility of performing ^{1}H NMR on picoliter-scale sample volumes in biological cells has been demonstrated using a 267-μm-diameter solenoid transceiver [7]. Additionally, using a combination of very strong gradients and a 73-μm-diameter solenoid, water voxels with corresponding volumes as low as 40 fL have been resolved in MR microscopy experiments [8]. While most of the work to date in micro-scale NMR has focused on solenoid-type microcoils wound around a capillary, in this article we examine another type of miniaturized NMR receiver coils: planar microcoils built using processes based on photolithography techniques derived from the semi-conductor industry, and referred to here as microfabrication or micromachining [9].

Photolithography allows fabrication of structures with features having a typical resolution of 1 μm. Thus, planar coils with sizes ranging from a few millimeters down to about 10 μm may be batch-fabricated with a degree of geometric precision and reproducibility, which is hardly achievable by winding a small conducting wire around a capillary. Another potential advantage of micromachined coils is the intrinsic compatibility for integration with chip-based microfluidic systems, often referred to as Micro Total Analysis Systems (μTAS) [10], allowing improved microscale fluidic handling and increased functionality. For a review of history, theory, technology and operation of μTAS systems, see [11,12].

* Corresponding author. Fax: +41-21-6936670.
E-mail address: charles.massin@epfl.ch (C. Massin).
[1] Now with Fluidigm Corp., CA, USA.

1090-7807/$ - see front matter © 2003 Elsevier Science (USA). All rights reserved.
doi:10.1016/S1090-7807(03)00151-4

Let us just mention here that considerable successful research has been performed on the integration of on-chip preconcentration and separations techniques, such as isotachophoresis, capillary electrophoresis (CE) and capillary electrochromatography (CEC). The on-chip combination of such techniques with NMR spectroscopy would be of great interest in an increasing number of applications [13]. Another prospective advantage of the planar geometry is the possibility for on-chip cell culturing [14], where biological cells would be attached directly at the surface of a planar coil, providing an optimal filling factor. This may in the future enable NMR screening within living cells, improving the drug discovery and design process [15,16]. Finally, microfabrication is easily amenable to produce arrays of planar microcoils and microfluidic channels, that would enable parallel spectrum acquisition and increased throughput, possibly surpassing what has already been demonstrated using solenoid microcoils [17,18].

In spite of initial research work having been performed early on [19,20], progress for planar microcoils in NMR has been much slower than for solenoid geometries. Stocker et al. [21] have reported the use of a susceptibility matching fluid to obtain high-resolution NMR spectra of liquid samples contained in a capillary positioned above a planar microcoil. They have shown an ^{1}H spectrum where peaks corresponding to $\sim$440 pmol of sucrose are clearly visible, obtained using a 60 μm planar coil with a 880 pL observe volume. This is remarkable given the extremely small amount of sample, but the resulting spectrum is not satisfactory neither in terms of signal-to-noise ratio (SNR) nor spectral resolution, compared to that obtained with solenoid microcoils. Trumbull et al. [22] have been the first to report an NMR spectrum obtained using an integrated device combining a planar microcoil with microfluidic channels. They have reported an ^{1}H spectrum of a 30 nL water sample acquired at 250 MHz with an SNR of 23.5 per scan, and a linewidth of 1.4 Hz. As noted by the authors, the low sensitivity due to the small filling factor and the highly resistive single-turn coil geometry has only allowed acquiring spectra at very high concentrations. Dechow et al. [23] have shown an ^{1}H NMR spectrum of 60 nL silicone-oil with a resolution of 100 Hz acquired at 500 MHz using a 1 mm diameter single-turn planar coil. The sample is placed in an open chamber, etched on the backside of the chip. A detailed analysis of the measured resolution and sensitivity is not available, but performance is clearly far from that achieved with solenoid microcoils.

A common problem of above-mentioned planar coils has been a high series resistance, resulting intrinsically in a low signal-to-noise ratio. Recently, we have reported an ^{1}H spectrum of ethylbenzene obtained with a 500-μm diameter planar coil having a series resistance of less than 1 Ω [24]. The volume of the sample contained in a capillary positioned above the microcoil is approximately 160 nL and the measured SNR is 20 for a single scan. That work has demonstrated the feasibility of fabricating planar microcoils with satisfactory electrical characteristics for measuring an NMR signal. However, the thick capillary walls result in a relatively low filling-factor, leaving many of the molecules in the capillary weakly contributing to the NMR signal. To alleviate this problem, we have integrated microfluidic channels in the substrate below the microcoil, and have acquired ^{1}H spectra of 30 nL water with a measured SNR of 120 per scan, demonstrating an improved sensitivity compared to previous experiments performed with planar microcoils [25]. We have also demonstrated the feasibility of performing MRI experiments using microfabricated planar coils and a water phantom [26].

In this article, we discuss and analyze in more detail the theory of micromachined NMR probes, and additional experimental results obtained with new probe geometries are presented. In the first part of Section 2, spatial sensitivity of planar microcoils is analyzed and expressions for time- and frequency-domain SNR are derived to allow comparison with the experiments. In the second part of Section 2, a model for predicting probe-induced distortions of the NMR spectrum is presented, enabling comparison of spectral linewidth between different probe geometries. In Section 3, the fabrication process, probe geometrical, and measured electrical characteristics are reported. NMR experiments are presented in Section 4, and results are compared to the theory, both for SNR and linewidth. Measurements performed with three different probe sizes enable verification of trends predicted by modeling. ^{1}H spectra of sucrose are successfully obtained for the first time with integrated probes. This leads to Section 5, where the current performance of micromachined NMR probes is reviewed and compared to that of other probe types. Based on the good agreement between theory and measurements, the future performance of micromachined NMR probes is extrapolated, and possible paths for improvement are discussed. With this contribution, we aim at reducing the current knowledge gap existing between the understanding of solenoid microcoils, extensively covered in the literature, and of planar microcoil-based NMR probes.

2. Theory

2.1. Sensitivity of planar microcoils

The signal amplitude obtained in an NMR experiment is closely related to the electromagnetic properties of the coils used for sample excitation and signal detection [27]. Here, we discuss the theoretical performance of microfabricated NMR probes schematically

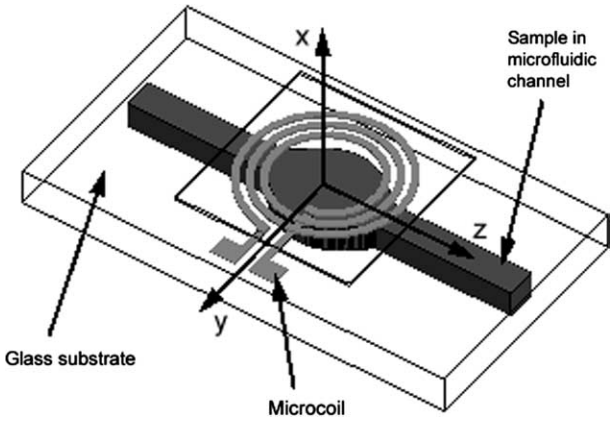

Fig. 1. 3D rendering of a micromachined NMR probe. The probe consists of a multi-turn electroplated planar microcoil integrated on a glass substrate with etched microfluidic channels for sample containment. The coil has typical dimensions of 2 mm or less, with sample-containment capability ranging from a few nanoliters to 1 μL, depending on coil size. As a reference valid throughout this article, the coil lies in the yz plane with the static magnetic field $\mathbf{B}_0$ along the z-axis.

represented in Fig. 1. As a convention valid throughout this article, the planar coil lies in the yz plane of the laboratory frame of reference, with the static magnetic field $\mathbf{B}_0$ along the z-axis. We consider the case where the same coil is used both for excitation and detection, which corresponds to our experimental conditions. For the purpose of quantifying the signal detected by a particular coil geometry, it is useful to introduce the unitary magnetic field $\mathbf{B}_{1u}(\mathbf{r}) = B_{1u,x}(\mathbf{r})\hat{\mathbf{x}} + B_{1u,y}(\mathbf{r})\hat{\mathbf{y}} + B_{1u,z}(\mathbf{r})\hat{\mathbf{z}}$, corresponding to the field produced by a DC current of 1 A flowing through the coil. The direction of the magnetic field $\mathbf{B}_{1u}(\mathbf{r})$ produced by a planar coil is plotted in Fig. 2 for points situated in the xz plane.

2.1.1. Sample excitation

During excitation, a current $i(t) = \hat{I}\sin(\omega t)$ flowing through the coil produces a linearly polarized alternating

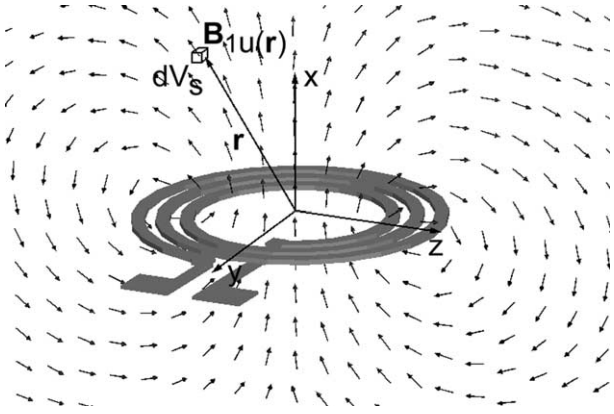

Fig. 2. Direction of the magnetic field $\mathbf{B}_{1u}(\mathbf{r})$ produced in the xz plane by a planar microcoil. Note that $B_{1u,y} = 0$ in the xz plane and that $B_{1u,x} = 0$ for points situated at large distance from the coil and at the "magic angle" (±54.7° with respect to the coil axis x).

magnetic field $\mathbf{B}_1(\mathbf{r},t) = \mathbf{B}_{1u}(\mathbf{r}) \cdot i(t)$. It can be shown that only half of the magnetic field $\mathbf{B}_1(\mathbf{r},t)$ produced by the coil has an effect on sample magnetization [28]. For each point $\mathbf{r}$ in the sample, we choose a local frame of reference $x'y'z'$ defined by the applied radio-frequency field (z'-axis along $\mathbf{B}_0$, and x'-axis positioned so that the y'-component of $\mathbf{B}_1(\mathbf{r},t)$ is zero). In the local frame, the effective component of $\mathbf{B}_1(\mathbf{r},t)$ perpendicular to $\mathbf{B}_0$ is along the x'-axis and equal to $B_{1e}(\mathbf{r}) = (\hat{I}/2) \cdot B_{1u,xy}(\mathbf{r})$, with $B_{1u,xy}(\mathbf{r}) = \sqrt{B_{1u,x}(\mathbf{r})^2 + B_{1u,y}(\mathbf{r})^2}$. In a pulsed NMR experiment, the net magnetization at equilibrium $\mathbf{M}_0$ is tilted from its original position along the z-axis by applying the magnetic field $\mathbf{B}_1(\mathbf{r},t)$ during pulse duration τ, at a frequency ω close to the Larmor frequency ω_0. Under ideal pulse conditions (i.e., $|\gamma B_{1e}| \gg |\omega_0 - \omega|$, $\tau \to 0$), the magnetization at point $\mathbf{r}$ is rotated by the following angle:

$$\theta(\mathbf{r}) = \gamma B_{1u,xy}(\mathbf{r})(\hat{I}/2)\tau. \tag{1}$$

Consequently, the transverse magnetization just after the excitation pulse is $M(\mathbf{r}) = M_0 \sin(\theta(\mathbf{r}))$ [29]. In the next paragraph, subsequent signal detection is discussed.

2.1.2. Signal detection

The voltage induced per elementary sample volume $\mathrm{d}V_s$ at position $\mathbf{r}$ (see Fig. 2) during detection is given by the principle of reciprocity [27]:

$$\xi(t,\mathbf{r}) = -\frac{\partial}{\partial t}(\mathbf{B}_{1u}(\mathbf{r}) \cdot \mathbf{M}(t,\mathbf{r})). \tag{2}$$

Evaluating expression (2) at time $t \ll T_2^*$ for the adopted orientation convention and single coil excitation–detection configuration, neglecting slowly varying terms and assuming perfectly homogeneous $\mathbf{B}_0$, yields the maximum amplitude of the signal envelope

$$\begin{aligned}\xi_0(\mathbf{r}) &= \omega_0 B_{1u,xy}(\mathbf{r}) M_0 \sin(\theta(\mathbf{r})) \\ &= \omega_0 B_{1u,xy}(\mathbf{r}) M_0 \sin(\gamma B_{1u,xy}(\mathbf{r})(\hat{I}/2)\tau).\end{aligned} \tag{3}$$

The signal contribution per elementary volume $\xi_0(\mathbf{r})$ (in Volts per cubic meter) is thus completely determined by the spatial distribution of $\mathbf{B}_{1u}(\mathbf{r})$ and the excitation parameters $\hat{I}$ and τ. The time-domain NMR signal $s(t)$ is obtained by integrating the signal density $\xi(t,\mathbf{r})$ over the whole sample volume V_s. Thus, the initial amplitude of the free induction decay (FID) is

$$\begin{aligned}S_0 = s(t)_{t=0} &= \int_{V_s} \xi_0(\mathbf{r})\,\mathrm{d}V_s \\ &= \int_{V_s} \omega_0 B_{1u,xy}(\mathbf{r}) M_0 \sin(\theta(\mathbf{r}))\,\mathrm{d}V_s.\end{aligned} \tag{4}$$

2.1.3. Specific properties of planar geometry

First, it is to be reminded that for planar coil geometries, the unitary magnetic field $\mathbf{B}_{1u}(\mathbf{r})$ is inhomogeneous both in amplitude and direction. To evaluate the

effect on the spatial sensitivity of planar microcoils, we compute the $\mathbf{B}_{1u}(\mathbf{r})$ field numerically using either a routine based on Biot–Savart law implemented in Matlab, or using a finite element analysis (FEM) software (Maxwell 3D, Ansoft corporation). For the FEM simulation, a complete 3D model of the NMR chip (including coil and microfluidic channel) is automatically generated within the design software (MEMS Pro, MEMSCAP S.A.) using mask layout information and a technology process file. The 3D model is then directly imported in the FEM software, which allows simulation of the exact fabricated device geometry.

The directional inhomogeneity of $\mathbf{B}_{1u}(\mathbf{r})$ is clearly visible in Fig. 2, obtained using the FEM method for a planar microcoil lying in the yz plane. A property of planar coils with circular symmetry is that for any plane containing the axis of symmetry, the magnetic field vector $\mathbf{B}_{1u}(\mathbf{r})$ is contained in that plane [31]. For example, the $B_{1u,y}$ component of $\mathbf{B}_{1u}(\mathbf{r})$ is null for any point in the xz plane as may be observed in Fig. 2. Therefore, the only component perpendicular to $\mathbf{B}_0$ in the xz plane is $B_{1u,x}$. Another characteristic is that the component of $\mathbf{B}_{1u}(\mathbf{r})$ parallel to the axis of symmetry vanishes at large distances from the coil for points situated on the surface of the so-called "magic angle cone" ($\pm 54.7°$ with respect to the axis of symmetry) [30]. In the example of the xz plane again, this means that for points situated at the magic angle, the $B_{1u,x}$ component is zero (see Fig. 2), and therefore the component perpendicular to $\mathbf{B}_0$ is null, implying undetected signal for portions of the sample situated at these positions.

$B_{1u,xy}(\mathbf{r})$ amplitude distribution depends directly on micromachined NMR probe geometrical parameters. The relevant parameters are illustrated in Fig. 3 and numerical values corresponding to the three probes geometries discussed in this article (probes A, B, and C) are given in the figure caption. As an example, the amplitude of $B_{1u,xy}(\mathbf{r})$ in the plane $x = -140\,\mu\text{m}$ (corresponding to the middle plane of the microfluidic channel) calculated using the Matlab script for probe A is plotted in Fig. 4. The field amplitude clearly varies strongly with spatial coordinates. The depressions observed along the z-axis correspond to regions of zero sensitivity (points situated at the "magic angle," see above). Another property clearly visible in Fig. 4 is that the $B_{1u,xy}(\mathbf{r})$ distribution has no circular symmetry with respect to the coil axis. Note how the amplitude of $B_{1u,xy}(\mathbf{r})$ diminishes more rapidly along the z-axis than along the y-axis. This results from the fact that the components of $\mathbf{B}_{1u}(\mathbf{r})$ transverse to $\mathbf{B}_0$ are not equal in the xz and xy planes [31]. These considerations should be taken into account when designing the microfluidic channel geometry and microcoil layout.

In order to quantify the NMR signal density $\xi_0(\mathbf{r})$, we have implemented a simple script in the FEM software calculating $\xi_0(\mathbf{r})$ based on the simulated value of $\mathbf{B}_{1u}(\mathbf{r})$. As an example, the resulting signal contribution per sample voxel of probe A is plotted in Fig. 5, for an excitation current and pulse duration producing a 90° flip angle in the middle of the sample chamber (at the position ($x = -140\,\mu\text{m}$, $y = 0$, $z = 0$)). Due to the inhomogeneous nature of the magnetic field $\mathbf{B}_{1u}(\mathbf{r})$, some portions of the sample may be excited with a flip angle $\theta(\mathbf{r})$ larger than 180°, giving a negative contribution to the total signal (see Eq. (4)). In Fig. 5, regions with null or negative signal contribution appear dark, while regions of high positive signal appear lighter. Note that for the presented probe geometry and excitation

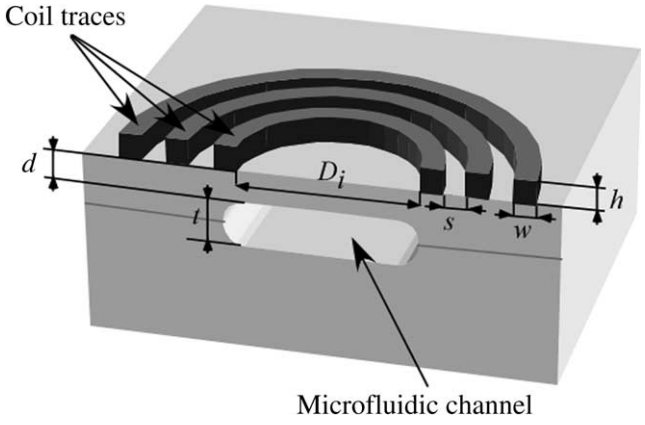

Fig. 3. Schematic section (xy plane) of a micromachined NMR probe encompassing a planar microcoil with N turns, inner diameter D_i, trace width w, trace height h, spacing between traces s, and a microfluidic channel of depth t etched in the substrate, with width equal to D_i and separated from the base of the coil traces by a distance d. Three different probes are tested in this article: probe A ($D_i = 500\,\mu\text{m}$, $N = 3$); probe B ($D_i = 1\,\text{mm}$, $N = 2$); probe C ($D_i = 2\,\text{mm}$, $N = 2$). For all three probes: $w = 40\,\mu\text{m}$, $h = 6\,\mu\text{m}$, $s = 30\,\mu\text{m}$, $t = 150\,\mu\text{m}$, and $d = 65\,\mu\text{m}$.

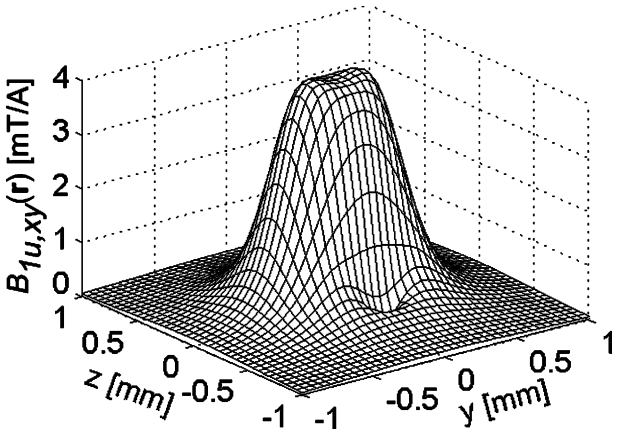

Fig. 4. Surface plot of $B_{1u,xy}(\mathbf{r})$ in plane $x = -140\,\mu\text{m}$ for probe A, obtained with a routine implementing Biot–Savart's law in Matlab. The maximum amplitude of $B_{1u,xy}$ in this plane is 4.4 mT/A, which is ~77% of the amplitude of the field at the coil center $B_{1u,xy}(x, y, z = 0)$. Note the depressions along the z-axis, corresponding to regions situated at the "magic angle." The sensitivity region extends further along the y-axis (perpendicular to $\mathbf{B}_0$) than the z-axis (parallel to $\mathbf{B}_0$).

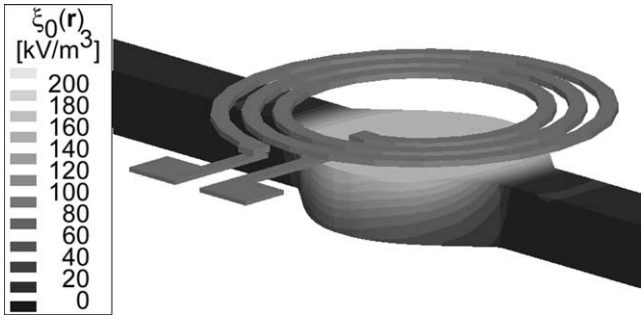

Fig. 5. Signal density distribution $\xi_0(\mathbf{r})$ for probe A, with excitation parameters $\tau = 10\,\mu s$ and $\hat{I} = 276\,mA$, corresponding to a 90° flip angle in the middle of the sample cavity (point (−140 μm, 0, 0)). The NMR signal is obtained using a script implementing Eq. (3) within the FEM software with the magnetic field value $\mathbf{B}_{1u}(\mathbf{r})$ calculated from the 3D model of the probe. Note that a cylinder of diameter equal to that of the coil approximates rather well the signal-contributing region.

parameters, the signal-contributing region is relatively well approximated by a cylinder having a diameter equal to the inner diameter of the coil and height equal to the channel depth.

2.1.4. Signal-to-noise ratio

For microcoils, where the noise is mainly due to the thermal noise generated by the series resistance R_c of the coil [1], the rms value of the time-domain noise is given by

$$\sigma_t = \sqrt{4kT_cR_cB}, \tag{5}$$

where R_c is the series resistance of the coil, T_c its temperature, and B the bandwidth in Hz of the detection electronics. Experimentally, the root-mean-square (rms) value of the noise σ is calculated taking M discrete samples of σ and using the relation

$$\sigma_{rms} = \sqrt{\frac{1}{M}\sum_k (\sigma_k - \langle\sigma\rangle)^2}. \tag{6}$$

We define the bandwidth-normalized, intrinsic time-domain SNR of the probe as

$$SNR_t = \frac{S_0}{\sqrt{4kT_cR_c}}. \tag{7}$$

Because this expression does not depend on spectral linewidth or shape, but only on probe characteristics, it illustrates that SNR is more easily predicted in the time domain than in the frequency domain. However, NMR signals are generally analyzed as spectra. Consequently, it is necessary to determine an expression for SNR in the frequency domain as well.

Considering a time-domain FID with an exponential decay envelope function $s^e(t) = S_0 e^{-t/T_2^*}$ for $t \geqslant 0$, the real part of the corresponding frequency-domain function obtained by Fourier transformation is a Lorentzian with maximum amplitude $A_0 = (1/2)T_2^* \cdot S_0$ and full width at half maximum (FWHM) $LW = 1/(\pi \cdot T_2^*)$ [29]. T_2^* is the apparent decay time, corresponding to the combined effects of T_2 relaxation and static field inhomogeneities.

The frequency-domain noise σ_f depends on the acquisition time T_{acq} and is given by the relation $\sigma_f = \frac{1}{\sqrt{2}}\sqrt{4kT_cR_c}\sqrt{T_{acq}}$. Therefore, the intrinsic frequency-domain SNR for a single acquisition is

$$SNR_f = \frac{S_0 \cdot T_2^*}{\sqrt{4kT_cR_c}\sqrt{2T_{acq}}} = SNR_t \cdot \frac{T_2^*}{\sqrt{2T_{acq}}}. \tag{8}$$

Since SNR in the frequency domain depends strongly on FID decay time T_2^*, static magnetic field inhomogeneities not only broaden spectral lines but also reduce SNR. If a matched weighting function $h(t) = e^{-t/T_2^*}$ is applied, SNR_f is proportional to $\sqrt{T_2^*}$ [29]. Compared to the intrinsic SNR, the output SNR is further reduced due to electrical interconnect losses, noise contribution of the preamplifier, and noise imaging in the mixer [32]. These factors are analyzed quantitatively in Section 4.

When calculating S_0 using Eq. (4), the amplitude of the magnetization at equilibrium is given by [33]

$$M_0 = \frac{N_s\gamma^2\hbar^2 I(I+1)B_0}{3kT_s}, \tag{9}$$

where T_s is the sample temperature and N_s the number of spins per unit volume. N_s is a function of both the number of molecules per unit volume and number of magnetically equivalent spins per molecule n_{eq}, and thus relates to the concentration C expressed in molar by the relation

$$N_s = 10^3 \cdot C \cdot N_A \cdot n_{eq}, \tag{10}$$

where N_A is Avogadro's number. For a pure water sample ($C = 55\,M$, $N_s = 6.6 \times 10^{28}\,m^{-3}$) at room temperature in a 7 T magnetic field, we find $M_0 = 0.022\,A/m$. To compare sensitivity performance of different probes, it is necessary to define appropriate figures of merit. In their review of small-volume NMR, Lacey et al. [34] define two different performance indicators: concentration and mass-related sensitivity. Similarly, we define here concentration-sensitivity per acquisition

$$S_c = \frac{SNR}{C \cdot N_{acq}^{1/2}}, \tag{11}$$

and mass-sensitivity per acquisition

$$S_m = \frac{SNR}{mol \cdot N_{acq}^{1/2}}, \tag{12}$$

where N_{acq} is the number of acquisitions. It is also useful to define the limit-of-detection (LOD), which is respectively the minimum concentration and minimum sample mass necessary for a given probe to yield an SNR of three in a single acquisition. Thus, $LOD_c = 3/S_c$ and $LOD_m = 3/S_m$.

2.2. Static field inhomogeneity

Nowadays, superconducting magnets are capable of achieving static magnetic field homogeneity on the order of a few parts per billion, so that the major source of distortion becomes the NMR probe itself [35]. Indeed, differences in bulk magnetic susceptibility of materials composing the probe create distortions of the static magnetic field. The problem is particularly severe with miniaturized probe, as many different materials are enclosed in a small volume in proximity of the sample [36]. Although NMR spectra with linewidths less than 2 Hz have been obtained and reported using microfabricated NMR probes [22], broadening of the resonance lines remain a significant issue. In this section, we discuss the influence of microfluidic channel geometry on NMR spectrum linewidth for integrated NMR probes, where the shape of the object under investigation is given by the geometry of the microfluidic channel used for sample containment.

2.2.1. Magnetism in NMR

We consider an object with homogeneous magnetic susceptibility $\chi \ll 1$ plunged in a perfectly homogeneous magnetic field $\mathbf{B}_0 = \mu_0\ \mathbf{H}_0$ (see Fig. 6). The externally applied magnetic field induces a magnetization $\mathbf{M} = \chi\ \mathbf{H}_0$ within the object due to its non-zero susceptibility, which in turn creates a demagnetizing field $\mathbf{H}_\mathrm{d}(\mathbf{r})$. The fields are related by the basic equation $\mathbf{H}(\mathbf{r}) = \mathbf{H}_0 + \mathbf{H}_\mathrm{d}(\mathbf{r})$ [37]. The external magnetic field $\mathbf{B}_0$ thus becomes a distorted and position-dependant field $\mathbf{B}(\mathbf{r}) = \mu_0(\mathbf{H}(\mathbf{r}) + \mathbf{M})$, yielding $\mathbf{B}(\mathbf{r}) = \mathbf{B}_0 + \chi\mathbf{B}_0 + \mu_0\mathbf{H}_\mathrm{d}(\mathbf{r})$. As a result, we may define the perturbation field:

$$\Delta\mathbf{B}(\mathbf{r}) = \mathbf{B}(\mathbf{r}) - \mathbf{B}_0 = \chi\mathbf{B}_0 + \mu_0\mathbf{H}_\mathrm{d}(\mathbf{r}). \tag{13}$$

The position dependence of the perturbation field is entirely determined by the demagnetizing field produced by the object, which in turn is related to its geometry and material composition. In particular, the demagnetizing field within objects having ellipsoid geometries is known to be homogenous and may be defined as $\mathbf{H}_\mathrm{d} = -N\ \mathbf{M}$, with N the demagnetization factor of the object. The sphere and long cylinder are special examples of ellipsoids with uniform demagnetizing fields, with N factors of 1/3 and 1/2, respectively [37]. For ellipsoid geometries, the perturbation field $\Delta\mathbf{B}(\mathbf{r})$ within the object is therefore theoretically uniform and given by $\Delta\mathbf{B}(\mathbf{r}) = \chi(1-N)\mathbf{B}_0$. In other geometries, the demagnetizing field is non-homogeneous and has to be calculated for each position in space $\mathbf{r}$. Different numerical techniques may be used to compute the distortion of the static magnetic field in NMR [30]. In this article, we make use of the FEM method (Maxwell 3D, Ansoft) as for the computation of $\mathbf{B}_{1u}(\mathbf{r})$. The FEM simulation results have been validated by comparison with that obtained using a C-computer program [38] implementing the surface integral technique [39].

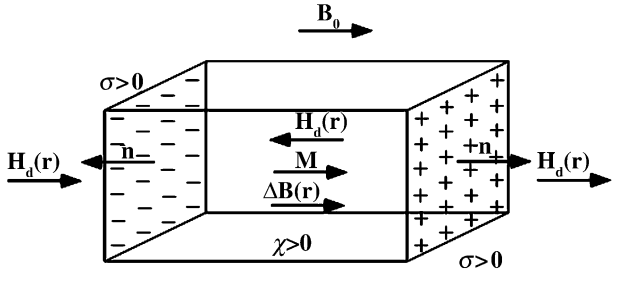

Fig. 6. Paramagnetic object plunged in a perfectly homogeneous external magnetic field $\mathbf{B}_0$. $\mathbf{M}$, magnetization induced within the object, due to its non-zero magnetic susceptibility χ; $\sigma = \mathbf{M}\cdot\mathbf{n}$, "equivalent magnetic charges" generated on the surface of the object; $\mathbf{H}_\mathrm{d}(\mathbf{r})$, demagnetizing field; $\Delta\mathbf{B}(\mathbf{r})$, perturbation field.

2.2.2. Probe modeling

We consider the NMR sample as an object having magnetic susceptibility $\Delta\chi$ given by the difference of magnetic susceptibility between the sample and substrate material, and whose shape is given by the microfluidic channel geometry in which it is enclosed, plunged in a perfectly homogeneous static magnetic field. Considering the particular channel geometry and coil sensitivity profile of the presented probes (see Figs. 1 and 5), we approximate the sample as being a cylindrical object with diameter equal to the inner diameter of the coil and height equal to the depth of the micromachined channel. For a pyrex glass substrate having magnetic susceptibility $\chi = -11\times10^{-6}$ and for a water sample of $\chi = -9\times10^{-6}$, the susceptibility difference is $\Delta\chi \approx +2\times10^{-6}$.

The resulting perturbation field for a cylinder with susceptibility $\chi = +2\times10^{-6}$, diameter over height ratio equal to 3.3 plunged in a homogenous static magnetic field $\mathbf{B}_0$ of magnitude 1 T along z-axis is plotted in Fig. 7. The plot shows both the direction of the perturbation field $\Delta\mathbf{B}(\mathbf{r})$ outside the sample (arrow plot) and its magnitude ΔB_z along z-axis within the sample (contour plot). The field in the central region of the cylinder is relatively homogenous, but shifted by a value approximately equal to $\chi\cdot B_0$ with respect to the applied magnetic field B_0. The main distortions occur in regions close to the object's edges in the direction of $\mathbf{B}_0$.

2.2.3. Distortion of the NMR spectrum

In the presence of a perturbation field $\Delta\mathbf{B}(\mathbf{r})$, the resonance frequency ω_0 becomes position-dependant: $\omega_0(\mathbf{r}) = \gamma|\mathbf{B}_0 + \Delta\mathbf{B}(\mathbf{r})| = \gamma|\mathbf{B}(\mathbf{r})|$ [28]. With the static magnetic field $\mathbf{B}_0$ along z-axis having z-component B_0, we have: $|\mathbf{B}(\mathbf{r})| = \sqrt{\Delta B_x(\mathbf{r})^2 + \Delta B_y(\mathbf{r})^2 + (B_0 + \Delta B_z(\mathbf{r}))^2}$. The ratio of the perturbation field $|\Delta\mathbf{B}(\mathbf{r})|$ over $|\mathbf{B}_0|$ is on the order of the magnetic susceptibility χ (see Eq. (13)), that is typically a few parts per million for most

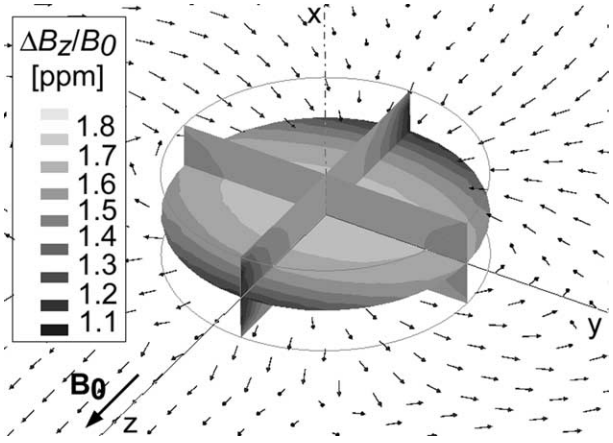

Fig. 7. Finite elements simulation of the static magnetic field within a cylindrical object of susceptibility $\chi = +2 \times 10^{-6}$ plunged in a 1 T homogenous external field. The cylinder diameter is 500 μm and height 150 μm (i.e., 3.3 ratio), and approximates the sensitive region of probe A (see Fig. 5). The field in the central region of the sample is shifted by a value corresponding to $\sim\chi \cdot B_0$, in accordance with Eq. (13). Note that regions of strong inhomogeneity gradients occur near the object's edges in the direction of $\mathbf{B}_0$.

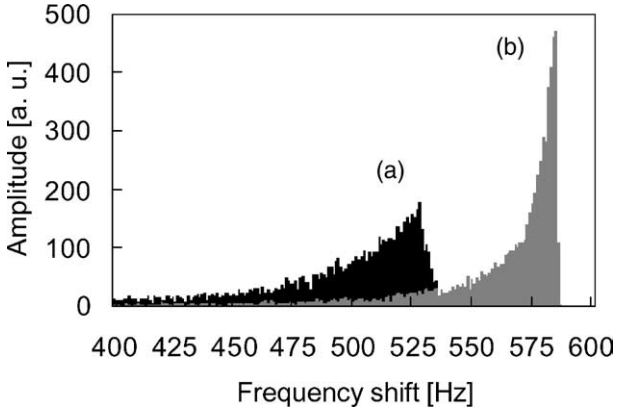

Fig. 8. Simulated NMR spectra for cylindrical samples with: (a) 3.3 and (b) 13.3 diameter over height ratios, corresponding respectively to probes A and C. The static field distribution is obtained from an FEM simulation of cylinders with magnetic susceptibility $\chi = 2 \times 10^{-6}$ plunged in a homogenous external magnetic field (see Fig. 7). Assuming homogeneous $B_{1u,xy}(\mathbf{r})$, the corresponding spectra are obtained by plotting a histogram of localized resonance frequencies, using $\Delta\nu = (\Delta B_z/B_0) \cdot \nu_0$, with $\nu_0 = 300$ MHz. The theoretical linewidths (FWHM) at 7 T are: (a) 30 Hz and (b) 10 Hz. Note that, in theory, spectral resolution improves with increasing diameter over height ratio.

non-ferromagnetic materials. From the previous considerations, it is clear that perturbations normal to $\mathbf{B}_0$ can be neglected and that the only distortion term to be considered is ΔB_z [30]. Thus, discrete sample volume elements at position $\mathbf{r}_k$ resonate at a frequency given by

$$\omega_0(\mathbf{r}_k) = \gamma(B_0 + \Delta B_z(\mathbf{r}_k)). \quad (14)$$

Assuming infinite T_2 relaxation time and homogenous $\mathbf{B}_1$ field, the effect of static magnetic field inhomogeneity on the NMR spectrum can be evaluated by plotting a histogram of localized resonance frequency with the corresponding expression given by $S(\omega) = \sum_k \delta(\omega - \omega_0(\mathbf{r}_k))$. This is a rather rough approximation, more elegant models are found in [40].

From theoretical considerations, it is expected that the homogeneity of the static field $\mathbf{B}(\mathbf{r})$ within different cylindrical geometries should vary depending on their respective diameter over height ratio. For cylinders with large diameter over height ratio, the field should be more homogenous than for cylinders with low ratio. Indeed, flat cylinders are close to ellipsoid geometries and therefore the demagnetizing field is more homogeneous.

Simulated spectra are plotted in Fig. 8 for two cylinders having diameter over height ratio of: (a) 3.3 and (b) 13.3, magnetic susceptibility $\chi = 2 \times 10^{-6}$ and plunged in a homogenous external magnetic field of 1 T. The theoretical linewidths FWHM for $B_0 = 7$ T are: (a) 30 Hz and (b) 10 Hz, obtained using $\Delta\nu = (\Delta B_z/B_0) \cdot \nu_0$, with $\nu_0 = 300$ MHz. The simulated resonance line for the flatter cylinder is narrower, in accordance with the previous general considerations. Note that this model assumes homogeneous $\mathbf{B}_1$ field in the sample chamber situated directly below the coil, and does not include signal contribution of the side channels. In future studies, $\mathbf{B}_0$ simulation in the entire microfluidic channel could be combined with $\mathbf{B}_1$ simulation (using the same FEM model as depicted in Fig. 5) to yield more accurate lineshape prediction.

3. Experimental

3.1. Probe fabrication

The NMR chips are batch-fabricated on 4-in. glass wafer substrates using micromachining. For general information about the microfabrication techniques involved, the interested reader is invited to consult one of the excellent books on the subject (see for example [9]).

The probe fabrication process flow is schematically represented in Fig. 9. Fabrication starts with processing of the microfluidic substrate, which is presented in detail in [41]. Channels are etched to a depth of 75 μm on the front side of two 525-μm-thick Pyrex-glass wafers, using hydrofluoric acid through a patterned poly-silicon layer mask. In addition, inlets and outlets holes are etched (or drilled in a modified process) on the backside of the bottom wafer to allow fluid injection in the probe (Fig. 9a). The two wafers are then aligned and fusion-bonded at ~600 °C forming a substrate with sealed microfluidic channels having symmetric cross-sections. To optimize coupling between the coil and NMR sample, the front surface of the wafer stack is thinned by mechanical polishing, leaving a 65 μm glass membrane over the 150-μm-deep channels (Fig. 9b).

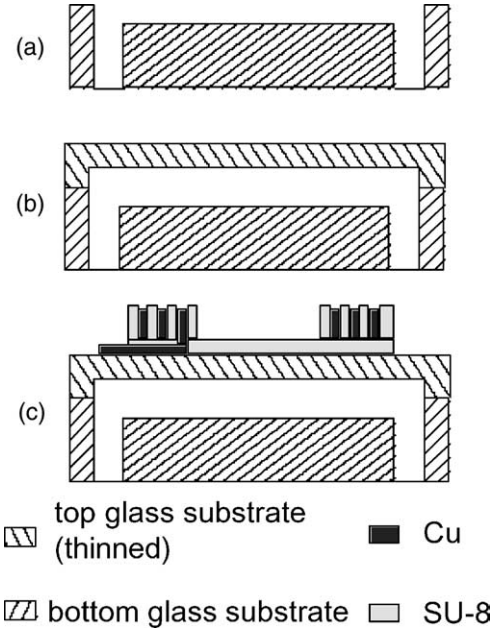

Fig. 9. Simplified fabrication process of planar microcoils on glass substrates with integrated channels. (a) Access holes and half channels (75 μm deep) are etched in the bottom substrate. (b) Half channels are etched in the top substrate, which is then fusion bonded to the bottom substrate. The top wafer is thinned down to a total thickness of 140 μm by polishing (75 μm chamber and channels, 65 μm membrane). (c) The planar coils are microfabricated using copper electroplating (see [24,41] for more information on process details).

The NMR detection coils are then integrated on the top surface of the microfluidic wafer stack, using a process based on SU-8 photoepoxy and copper electroplating (Fig. 9c) described in detail in [24]. The coils positioning with respect to the microfluidic channels is performed in a parallel fashion, by mask alignment to dedicated marks patterned in the fluidic substrate. Once the coil fabrication process is terminated, the electrical impedance of the coil is measured using coplanar RF probes (Picoprobes, GGB Industries). The measured electrical characteristics at 300 MHz are reported in Table 1. Finally, the wafer is diced resulting in the individual NMR chips. A micromachined NMR chip is pictured in Fig. 10. Fluidic connectors and tubes used for sample injection are also visible on this picture. Detailed views of detection microcoils are shown in Fig. 11.

Table 1
Measured coil electrical characteristics at 300 MHz for the tested NMR probes

Probe	D_i (μm)	L (nH)	R_c (Ω)	Q
A	500	8.8	1.0	17
B	1000	8.8	0.9	18
C	2000	19.8	2.0	19

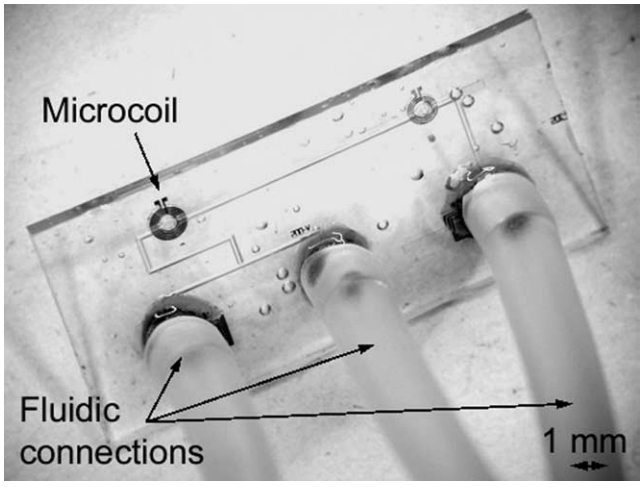

Fig. 10. Picture of a micromachined planar NMR probe. The glass chip has a size of $(16 \times 8)\,mm^2$. The visible microfluidic channels have a width of approximately 170 μm. The pointed microcoil has an inner diameter of 500 μm, and an observe volume of 30 nL. The sample is injected via flexible plastic tubes connected to inlet and outlet holes on the backside of the chip. Note that several coils may easily be integrated on a single chip.

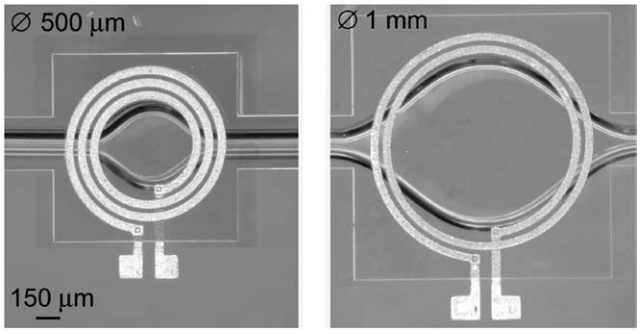

Fig. 11. Detailed view of two different detection microcoils, with 500 μm (probe A, left) and 1 mm (probe B, right) inner-diameters. In both cases, the channel depth is 150 μm, resulting in respectively 30 and 120 nL observe sample volumes.

3.2. Interconnect and measurement setup

To perform NMR measurements, the chip must be interconnected to the "macro world." Fluidic connectors are glued on the backside of the chip, directly opposite to the 1 mm diameter inlet and outlet holes (see Fig. 10). The glass chip is then glued to a printed circuit board (PCB) with through-holes, allowing access to the fluidic connectors located on the backside. Flexible PVC tubes with 1 mm inner diameter are slipped on the fluidic connectors, providing a leak-free fluidic connection to the chip. The microcoil is electrically connected to the board's upper face copper traces using 30 μm diameter aluminium wire bonding. Each bonding wire has an estimated length of 3 mm. The coil is tuned and matched to 50 Ω at 300 MHz using a conventional parallel-series

capacitors scheme [2]. Non-magnetic SMD trimmer-capacitors (CTZ3 type, AVX) are soldered on the PCB a few mm away from the coil. A flexible coaxial cable soldered to the PCB provides the electric connection to the electronics setup. Sample loading is performed outside of the superconducting magnet, after which the micromachined probe is inserted in the magnet's room-temperature bore. NMR measurements are carried out using two different setups. The first one is a home-built spectrometer (see [24]). The noise figure of the preamplifier is ~2 dB. This setup has no room-temperature shimming system. In order to test the effect of shimming on spectral resolution, additional measurements are performed in a conventional commercial NMR spectrometer (Bruker DRX 300, Bruker Biospin AG).

4. Results

4.1. Measured performance with a water sample

4.1.1. Time-domain SNR

The sensitivity performance of micromachined probes is measured and compared with the values predicted using the model described in Section 2 (Eq. (4)), by measuring the NMR signal amplitude S_0 in the time-domain versus excitation pulse duration τ, for a water sample with a single acquisition using the home-built spectrometer. The planar microcoil is used for both sample excitation and signal detection. Assuming a perfectly lossless tuning and matching network, all active power applied to the probe terminals is dissipated in the series resistance of the coil R_c, i.e., $P = R_c\hat{I}^2/2$. $\hat{I}$ may thus be determined from the previous relation, and introduced in Eq. (4) for comparison with the model. During detection, assuming that the detection coil is perfectly tuned and matched (with lossless capacitors) to 50 Ω, a voltage signal of amplitude $(1/2)\sqrt{50/R_c}\cdot S_0$ appears at the preamplifier input terminals. Thus for probe A, the measured value at the preamplifier input must be divided by a factor ~3.5 for comparison with the model. The experimental result (dots) and the simulated values (continuous line) at the coil terminals are plotted in Fig. 12 for probe A. The simulated value is obtained by integration of the signal density $\xi_0(\mathbf{r})$ over the whole sample volume (see Fig. 5) for different excitation pulse durations τ. The simulated maximum signal amplitude is 5 μV for $\tau = 10$ μs. The maximum signal amplitude found experimentally at the preamplifier input terminals is 14 μV for $\tau = 10$ μs, corresponding to a value of 4 μV at the coil terminals (gain of resonant circuit). To account for the difference, the bonding wires resistance R_b must be taken into consideration. When doing so, the resonant circuit gain is reduced by a factor $\sqrt{1 + (R_b/R_c)}$. The additional resistance per wire is estimated to be 0.2 Ω at 300 MHz, yielding $R_b = 0.4\,\Omega$. For probe A ($R_c = 1\,\Omega$), this corresponds to signal attenuation by a factor of 1.2. Considering this factor, there is very good agreement between the simulated and experimental values.

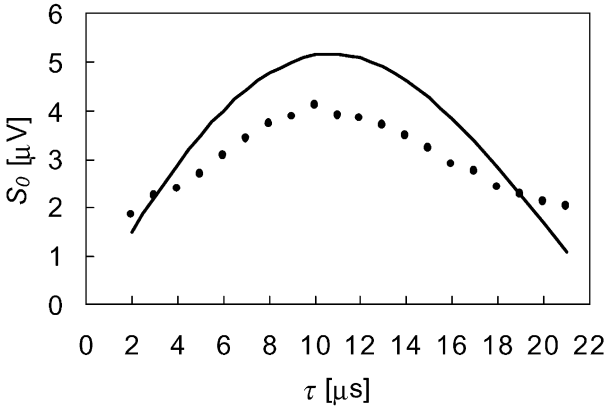

Fig. 12. Measured (dots) and theoretical (continuous line) ^{1}H NMR signal amplitude S_0 at the microcoil terminals versus excitation pulse duration τ for probe A. Experimental conditions: $B_0 = 7$ T, 30 nL water sample, excitation power $P = 38$ mW. The theoretical value is obtained using a 3D model of the probe (see Fig. 5) and solving Eq. (4) in the FEM software for the excitation current amplitude $\hat{I} = 276$ mA, derived from the experimental conditions using the relation $P = R_c\hat{I}^2/2$. The amplitude at the coil terminals is obtained by dividing the measured signal amplitude by the total gain of the detection chain without fitting parameters.

The equivalent rms noise value at the input terminals of the preamplifier is calculated using Eq. (6) for 100 measured data points, which divided by the gain of the detection chain gives $\sigma_t \approx 200$ nV. The effective bandwidth of the filter is $(2\pi/4)30 \times 10^3$ Hz, yielding an input noise of 0.9 nV Hz$^{-1/2}$. The resulting experimental SNR value for probe A is $\mathrm{SNR}_t \approx 15 \times 10^3\,\mathrm{Hz}^{1/2}$ for one acquisition. For a pure water sample, the intrinsic time-domain SNR at the coil terminals predicted for probe A using Eq. (7) with $R_c = 1\,\Omega$, is $\mathrm{SNR}_t \approx 39 \times 10^3\,\mathrm{Hz}^{1/2}$. Considering the signal attenuation due to the bonding wires, noise figure of the preamplifier (2 dB), and noise imaging of the mixer (3 dB), the intrinsic value must be divided by a factor 2.1 for comparison with the measurement. The experimental value of $\mathrm{SNR}_t \approx 15 \times 10^3$ $\mathrm{Hz}^{1/2}$ is thus 17% smaller than the value of 18×10^3 $\mathrm{Hz}^{1/2}$ predicted by theory for the output SNR. Similar experiments are repeated with probes B and C, and the corresponding results are listed in Table 2, together with the mass-sensitivity S_m calculated for the three different probes using Eq. (12). It is found experimentally that the mass-sensitivity increases linearly with the inverse of coil diameter D_i (i.e., $S_m \propto D_i^{-1}$).

4.1.2. Spectral resolution and frequency-domain SNR

The spectral performance is assessed for probe A by taking the real part of the Fourier transform of the measured FID obtained in the conditions of Fig. 12 with

Table 2
Tested micromachined NMR probes time-domain characteristics

Probe	V_s (nL)	S_0 theory (μV)	S_0 meas. (μV)	SNR_t intrinsic (10^3 $\sqrt{Hz}$)	$SNR_{t,out}$ theory (10^3 $\sqrt{Hz}$)	SNR_t meas. (10^3 $\sqrt{Hz}$)	$S_{m,t}$ meas. (10^3 $\sqrt{Hz}\,\mu mol^{-1}$)
A	30	5	4	39	18	15	9.1
B	120	10	7	82	38	28	4.2
C	470	29	22	159	81	60	2.3

Data are valid for a single acquisition at 300 MHz.

$\tau = 10\,\mu s$. The resulting spectrum (dots) is plotted in Fig. 13 together with a Lorentzian fit with 30 Hz FWHM linewidth (broken line). The corresponding value of the apparent relaxation time is $T_2^* \approx 10$ ms. This is much smaller than the known transverse relaxation time of water $T_2 \sim 2.8$ s [33]. In Section 2, a linewidth of ~30 Hz has been predicted for probe A at 7 T by modeling the sample as a cylindrical object plunged in a perfectly homogeneous magnetic field (see Figs. 7 and 8(a)). The model is in good agreement with the experimental data (using $LW = 1/\pi T_2^*$) and the large broadening of the natural resonance line may thus in the first order be explained as a result of static magnetic field distortions introduced by the integrated probe fluidic channel geometry.

The spectrum of Fig. 13 is also used to evaluate frequency-domain SNR. The experimental value is obtained by dividing the peak amplitude by the rms noise, obtained from the measured data using Eq. (6); this yields $SNR_f = 260$. The frequency-domain SNR predicted by Eq. (8) for the corresponding experimental conditions is $SNR_f \approx 680$, with $T_2^* = 10$ ms and $T_{acq} = 164$ ms. As pointed out for time-domain SNR, this intrinsic value should be divided by a factor 2.1 (preamplifier noise figure, bond wire losses, and noise imaging of the mixer) for comparison with the measured data. Consequently, the measured value of 260 is ~20% smaller than the predicted number of 320.

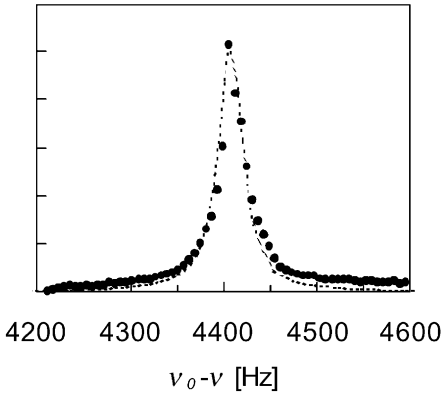

Fig. 13. ^{1}H NMR spectrum (real part, dots) of a 30 nL water sample measured using probe A and Lorentzian fit with FWHM = 30 Hz (broken line). Experimental conditions: $B_0 = 7$ T, $P = 38$ mW, $\tau = 10\,\mu s$, $B = 30$ kHz, $T_{acq} = 164$ ms, three acquisitions. Measured $SNR_f \approx 260$ per scan.

4.2. Measured performance with a sucrose sample

To further evaluate sensitivity and spectral resolution, ^{1}H spectra of sucrose have been acquired using probe A and C (see Fig. 14). The commercial spectrometer used for these experiments includes a quadrature detection scheme, suppressing noise imaging at the mixer and theoretically yielding an increase in SNR by a factor $\sqrt{2}$ compared to the home-built spectrometer [32]. To ensure a sufficient signal, sucrose has been prepared at a concentration of 1 M in D_2O. The frequency-domain SNR is measured on the anomeric proton ($\delta \approx 5.3$ ppm). Compared to a pure water sample, the

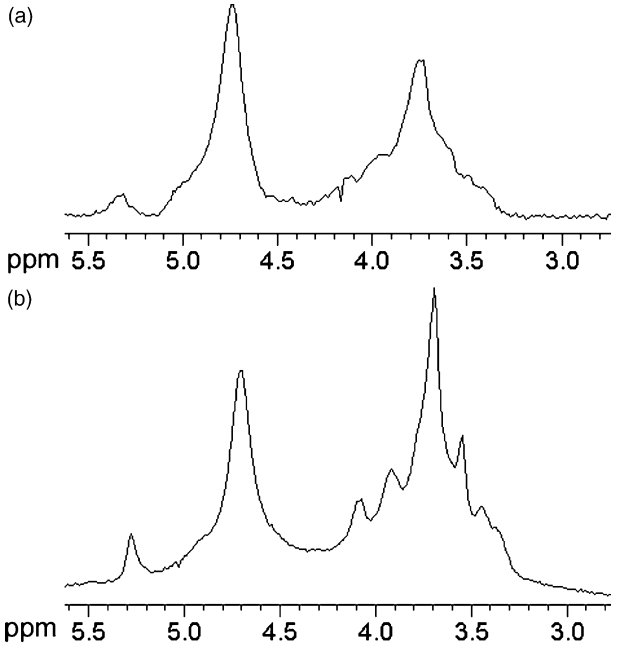

Fig. 14. ^{1}H spectra of 1M-sucrose concentration in D_2O acquired at 300 MHz using micromachined NMR probes. (a) Spectrum acquired using probe A, with sample volume ~30 nL (diameter over height ratio 3.3). The corresponding sample mass is 10 μg (30 nmol). Measured $SNR_f \approx 14$ (anomeric proton), for 24 acquisitions, $B = 2$ kHz, $T_{acq} = 0.4$ s. (b) Spectrum acquired using probe C, with sample volume ~470 nL (diameter over height ratio 13.3). The corresponding sample mass is 160 μg (470 nmol). Measured $SNR_f \approx 48$ (anomeric proton), for 16 acquisitions, $B = 1.6$ kHz, $T_{acq} = 0.5$ s.

spin density is $N_s = 6 \times 10^{26}\,m^{-3}$, reducing sample magnetization by a factor ~100. The spectrum acquired using probe A (Fig. 14(a)) has a measured $SNR_f = 14$ with 24 acquisitions, for an observe sample volume of 30 nL and corresponding sample amount of 10 μg (30 nmol). This yields a signal-to-noise ratio of ~3 per acquisition. This is in good agreement with the value of ~3.3 that would be extrapolated based on the experimental value obtained with the water spectrum of Fig. 13. The intrinsic value predicted based on Eq. (8) is ~4, with $T_2^* = 10$ ms and $T_{acq} = 0.4$ s.

For probe C (Fig. 14(b)), which has an observe volume of 470 nL, the measured value is $SNR_f = 48$ for 16 acquisitions. This yields an SNR of ~12 per acquisition for 160 μg (470 nmol) of sample. An estimation based on Eq. (8) with $T_2^* = 16$ ms and $T_{acq} = 0.5$ s would yield a signal-to-noise ratio ≈23. The results are summarized in Table 3, and allow direct comparison between the two micromachined probes. In accordance with the results obtained in the time-domain for the water sample, the mass-sensitivity S_m is again found to increase linearly with the inverse of coil dimensions. Indeed probe A, with a coil diameter of 500 μm and 30 nL sample volume shows a 4-fold increase in mass-sensitivity compared to probe C, which has a coil diameter of 2 mm and 470 nL sample volume. Concentration limit of detection is currently on the order of 0.25 M for a single scan with probe C. Unlike mass-sensitivity; concentration-sensitivity becomes poorer as the coil size is reduced.

Next, the two spectra of Fig. 14 are compared in terms of spectral resolution. It is observed that the spectrum obtained with probe C has a better resolution than that obtained with probe A. The two experimental spectra should be compared to that of Fig. 8, where spectral line shape is calculated for both probes by simulation of the static magnetic field distortion in a cylindrical sample. As expected (see Section 2), the probe with the larger coil diameter over channel height ratio has the better resolution. Also, while room temperature shimming does not improve resolution for probe A, it is partially effective for probe C. Given the sufficiently high SNR of the spectrum of Fig. 14b, a Lorentz–Gauss transformation [29] is applied to the original FID to yield a spectrum with a resolution less than 10 Hz, and an SNR of ~10 per acquisition (Fig. 15). This demonstrates that the spectral information is present in the original signal, and may be recovered with the appropriate signal processing.

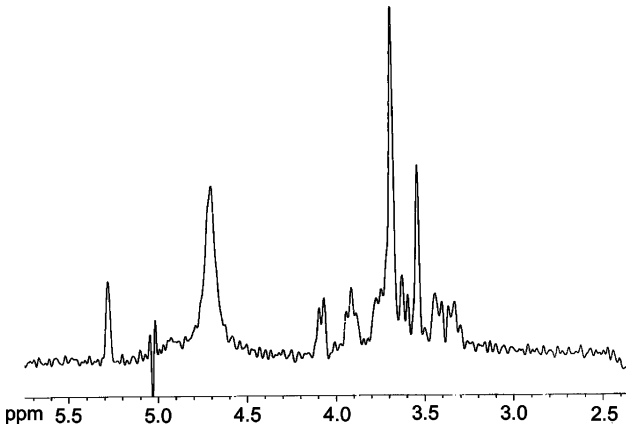

Fig. 15. ^{1}H spectrum of 160 μg sucrose in 470 nL D_2O, corresponding to that of Fig. 14(b) after Lorentz–Gauss resolution enhancement [29]. The original FID data is multiplied by the weighting function $h(t) = e^{(t/T_2^* - \sigma^2 t^2/2)}$, with $T_2^* = 16$ ms and $\sigma^2 = 628$. The resulting spectrum has a Gaussian lineshape with FWHM ~9 Hz and $SNR_f \sim 38$ (anomeric proton), for 16 acquisitions.

5. Discussion

The results reported in the previous section are summarized below and put in perspective by comparison with theory, previously published data on planar microcoils, and performance of other NMR probes.

5.1. Current performance of micromachined NMR probes

It is found from data reported in Tables 2 and 3 that the modeling and methodology described in the theory section enable prediction of the absolute SNR obtained for a particular micromachined NMR probe within a factor of two compared to the experimental value, both in the time and frequency-domains. Measured sensitivity performance is therefore considered in good agreement with theoretical expectations. The difference is explained as a result of the model not taking into account non-idealities such as interconnect losses due to PCB traces, and capacitors losses. An improved model should consider these effects, as has been done for solenoid microcoils [4]. By comparison of the relative performance between different probes, the increase of mass-sensitivity with coil diameter reduction is demonstrated experimentally for planar microcoils. For the probe geometries considered, it is found that S_m varies as D_i^{-1}. This justifies efforts to build planar coils with reduced

Table 3
Spectral performance of micromachined NMR probes as measured at 300 MHz with a 1 M-sucrose sample concentration in D_2O, for a single acquisition

Probe	Sample mass (μg)	Sample amount (μmol)	T_2* (ms)	SNR_f intrinsic Eq. (8)	SNR_f meas.	$S_{m,f}$ meas. (μmol^{-1})	LOD_m meas. (nmol)	LOD_c meas. (M)
A	10	0.03	10	4	3	100	30	1
C	160	0.47	16	23	12	26	115	0.25

sizes for analysis of mass-limited samples. On the other hand, a probe with a small observe-volume clearly has a worse concentration sensitivity than a probe with a large observe-volume. Depending on the intended application, concentration limit of detection may ultimately determine the minimum usable coil size.

The measured poor spectral resolution (i.e., linewidths $\gg 1$ Hz) is in accordance with results obtained from simulation (see Fig. 8). The proposed model allows relatively good quantitative prediction at this order of magnetic field inhomogeneity. Directions for improvement suggested by simulation prove correct, as demonstrated experimentally with the spectra plotted in Fig. 14. The probe with the larger coil diameter over channel depth ratio has indeed a better spectral resolution. In light of these considerations on the effect of channel geometry on linewidth, we interpret the excellent spectral resolution obtained by Trumbull et al. [22] as a consequence of the sample chamber geometry, which had a width of 1 mm and a depth of 30 μm, resulting in an aspect ratio of ~33, compared to an aspect ratio of 13 for probe C. This emphasizes the importance of having microfluidic channels with a shape approaching an ellipsoid geometry in the sensitive region of the detection coil, in order to avoid this cause of line broadening. Also, we conclude that for the probes tested here, the sample shape is the main source of linewidth enlargement. Other potential sources of static field distortions such as the coil wire and dielectric spacing layer have not been considered in this article, but they can straightforwardly be included in the FEM simulation for future optimization. The large broadening of resonance lines observed for the presented micromachined probes is currently the main factor limiting their performance for high-resolution applications.

5.1.1. Comparison between planar microcoil-based probes

In spite of the comparatively good spectral resolution obtained by Trumbull et al. [22], the SNR measured here with probe A is approximately an order of magnitude larger than that they have reported for the same sample volume. Dechow et al. [23] have not reported SNR, but we estimate to be around 6 per scan, considerably lower than that measured with our probes for a water sample. Previously, we have acquired an ^{1}H spectrum of 160 nL ethylbenzene contained in a capillary positioned above a 500 μm diameter planar coil (same coil geometry than in probe A) [24]. The corresponding mass-sensitivity of ~15 μmol^{-1} was ~6 times lower than that reported here for probe A, due to the thick capillary walls resulting in a relatively low filling-factor. Consequently, in our opinion, the ^{1}H spectrum of 160 μg sucrose shown in Fig. 15 illustrates the current state-of-the-art performance reached using micromachined probes. Due to the current poor spectral resolution, this spectrum has required resolution-enhancement processing, illustrating the possible trade-offs between SNR and spectral resolution.

5.1.2. Comparison with other types of NMR probes

In their review, Lacey et al. [34] have compared several NMR probes at 600 MHz. They have not included planar microcoil probes in their comparison, because at that time they have judged their sensitivity as too low. Among spectra acquired with micromachined NMR probes to date, we consider the sucrose spectrum of Fig. 15 as the most appropriate to attempt a first meaningful comparison with other NMR probes from an experimental point-of-view. Given that results presented here are obtained at 300 MHz, normalization is required for appropriate comparison. The NMR signal amplitude varies as a function of B_0^2 (see Eqs. (3) and (9)). Due to skin effect, the resistance of the coil is considered as varying as the square root of frequency. Consequently, SNR is proportional to $B_0^{7/4}$ [27]. For probe C and assuming constant linewidth, the mass-sensitivity at 600 MHz would therefore be $S_m = 88$ μmol^{-1}. For a conventional 5-mm probe, Lacey and co-authors reported a measured SNR of 136 on the anomeric proton, obtained for a single scan of a 0.5 μmol sucrose sample quantity. Using Eq. (12), this represents a mass-sensitivity of 272 μmol^{-1}. Therefore to date, the experimental sensitivity of planar microcoils compared on a meaningful spectrum is still a factor 3 smaller than obtained with a conventional high-resolution probe. However, there is great potential for improvement, which we discuss in the next paragraphs.

5.2. Future performance of micromachined NMR probes

The most detrimental drawback of the micromachined probes presented in this article is their poor spectral resolution. This not only prevents observation of fine spectral features, but also severely impairs sensitivity in the frequency-domain. Considering Eq. (8), if the FID decay is decreased from a value of 1 s to a value of 10 ms due to field inhomogenetities, frequency-domain SNR is reduced by a factor of 10. Now, based on the results obtained in this article, let us investigate the projected performance of micromachined NMR probes once the $\mathbf{B}_0$ inhomogeneity problem is solved. Considering probe C in the conditions of Fig. 14, if the linewidth were reduced from 20 to 0.7 Hz with an increase of acquisition time from 0.5 s to 4 s, this would generate a 10-time increase in sensitivity, yielding $S_m = 260$ μmol^{-1} at 300 MHz. This value has to be scaled to 600 MHz for comparison with published data. Recent improvements in coil fabrication process have allowed further reducing series resistance, and since coil resistance is involved in the scaling calculation, we take the measured resistance value at 600 MHz of the same coil C, but fabricated with the improved process: $R_c = 1.3\,\Omega$. Therefore, mass-sensitivity at 600 MHz for improved probe C would be S_m ~1290 μmol^{-1}. Again comparing with data published in [34], this would now result in a

5-fold mass-sensitivity improvement over the 5-mm conventional NMR probe ($S_m = 276\,\mu mol^{-1}$), and leading the sensitivity of probe C to be a factor two smaller than that reported for a solenoid microcoil with 620 nL observe sample volume. Now, considering the demonstrated linear sensitivity versus size improvement between micromachined probes discussed in this article (see Table 3), probe A would achieve a mass-sensitivity of $\sim 5200\,\mu mol^{-1}$ for an observe volume of 30 nL, a $\sim$20-fold improvement when compared to a conventional 5-mm NMR probe. These exciting prospects provide the motivation to tackle the challenge of micromachined probe-induced static magnetic field dishomogeneity. SNR might also be increased by ways of improved coil geometries. For example, based on this technology, it would be feasible to introduce a second coil underneath the sample yielding a coil arrangement resembling a Helmholtz configuration.

5.2.1. Possible paths for spectral resolution improvement

Regarding the problem of micromachined probe-induced static field distortions, we have identified possible improvements along three different paths: probe design and materials, shimming and signal processing. With regards to probe design, ellipsoid geometries and increased symmetry, coupled with susceptibility-controlled materials [30] should improve the situation. Microfabrication should represent an advantage along that direction, due to the precise control of material deposition and geometries and a high degree of reproducibility. An additional possibility is the use of susceptibility-matching fluid [19]. Next, it has been noted that conventional room-temperature shimming is rather ineffective for micromachined probes, because it is unable to compensate for strong magnetic field gradients. Development of dedicated shimming gradients, dubbed here micro-shimming, might prove a viable approach. Finally, if no hardware development proves successful, the broadened spectra may be corrected post-acquisition with adequate signal processing. In particular reference deconvolution has proved particularly effective in similar cases [42,43].

6. Conclusions

In this article, an ^1H spectrum of 160 μg sucrose in D_2O acquired with a micromachined planar NMR probe having a 470 nL observe volume is presented. This spectrum is representative of the current performance of planar microcoil-based NMR probes. The intrinsic sensitivity of the presented probes is significantly improved compared to previously published planar microcoils work. A model based on the principle of reciprocity and 3D FEM simulation is presented that allows prediction of absolute probe sensitivity within a factor of two compared to the experimental data, without fitting parameters. This validates a design methodology that enables quantitative prediction and optimization of probe performance based on a 3D model automatically extracted from the fabrication mask layout, applicable to arbitrary planar geometries. Comparison of relative performance between three different micromachined planar probes demonstrates experimentally the increase of mass-sensitivity with coil diameter reduction. Analysis of the results and confirmation through the model show that probe-induced static field perturbations severely reduce frequency-domain sensitivity. As a consequence, the present performance of micromachined probes is poor compared to other high-resolution NMR probes. Currently, this relegates microfabricated probes to applications where the natural linewidth of the sample under investigation is larger than probe-induced broadening, or where magnetic field inhomogeneity is caused by the static field source itself, such as in low-field NMR spectrometers employing permanent magnets. However, paths for improvement of spectral resolution are identified. A prediction based on the presented model show that future performance of planar-microcoil based NMR probes for high-resolution applications may approach that of solenoid microcoils for observe volumes around 500 nL or less, with the additional advantages related to planar-chip based technology. This would enable the appearance of a new generation of miniaturized analytical devices combining on-chip separation and NMR detection within the magnet bore.

Acknowledgments

The devices were fabricated in the SAMLAB (IMT, University of Neuchâtel) cleanroom and at the Center of Microtechnology (CMI) at EPFL. We thank the technical staff of both centers, as well as Y. Pilloud, G. Vaucher, and V. Gfeller for helpful support. We acknowledge J. Abenhaim for the Matlab© routine. We thank Prof. G. Bodenhausen and his collaborator M. Rey at EPFL for spectrometer access and their active support in acquisition of the sucrose spectra. This work was supported by an EPFL Presidential Fund (IMD-EPFL scholarship) and by the Swiss National Science Foundation (Project No. 2100-61549.00).

References

[1] T.L. Peck, R.L. Magin, P.C. Lauterbur, Design and analysis of microcoils for NMR microscopy, J. Magn. Reson. B 108 (2) (1995) 114–124.
[2] A.G. Webb, Radiofrequency microcoils in magnetic resonance, Prog. Nucl. Magn. Reson. Spectrosc. 31 (1997) 1–42.

[3] K.R. Minard, R.A. Wind, Solenoidal microcoil design. Part I: Optimizing RF homogeneity and coil dimensions, Concepts Magn. Reson. 13 (2001) 128–142.
[4] K.R. Minard, R.A. Wind, Solenoidal microcoil design. Part II: Optimizing winding parameters for maximum signal-to-noise performance, Concepts Magn. Reson. 13 (2001) 190–210.
[5] D.L. Olson, T.L. Peck, A.G. Webb, R.L. Magin, J.V. Sweedler, High-resolution microcoil 1H-NMR for mass-limited, nanoliter-volume samples, Science 270 (5244) (1995) 1967–1970.
[6] S.S.C. Grant, N.R. Aiken, H.D. Plant, S. Gibbs, T.H. Mareci, A.G. Webb, S.J. Blackband, NMR spectroscopy of single neurons, Magn. Reson. Med. 44 (2000) 19–22.
[7] K.R. Minard, R.A. Wind, Picoliter ^{1}H NMR spectroscopy, J. Magn. Reson. 154 (2002) 336–343.
[8] L. Ciobanu, D.A. Seeber, C.H. Pennington, 3D MR microscopy with resolution 3.7 μm by 3.3 μm by 3.3 μm, J. Magn. Reson. 158 (2002) 178–182.
[9] M. Madou, Fundamentals of Microfabrication, CRC Press, Boca Raton, 1997.
[10] A. Manz, N. Graber, H.M. Widmer, Miniaturized total chemical analysis systems: a novel concept for chemical sensing, Sensor. Actuat. B 1 (1990) 244–248.
[11] D.R. Reyes, D. Iossifidis, P.-A. Auroux, A. Manz, Micro total analysis systems. 1. Introduction, theory, and technology, Anal. Chem. 74 (2002) 2623–2636.
[12] P.-A. Auroux, D. Iossifidis, D.R. Reyes, A. Manz, Micro total analysis systems. 2. Analytical standard operations and applications, Anal. Chem. 74 (2002) 2637–2652.
[13] A.K. Malik, W. Faubel, A review of capillary electrophoretic separations and their studies by nuclear magnetic resonance, J. Capillary Electrop. Microchip Technol. 6 (3/4) (1999) 97–108.
[14] I. Inoue, Y. Wakamoto, H. Moriguchi, K. Okano, K. Yasuda, On-chip culture system for observation of isolated individual cells, Lab Chip 1 (2001) 50–55.
[15] B.J. Stockman, C. Dalvit, NMR screening techniques in drug discovery and drug design, Prog. Nucl. Magn. Reson. Spectrosc. 41 (2002) 187–231.
[16] Z. Serber, A.T. Keatinge-Clay, R. Ledwidge, A.E. Kelly, S.M. Miller, V. Dötsch, High-resolution macromolecular NMR spectroscopy inside living cells, J. Am. Chem. Soc. 123 (2001) 2446–2447.
[17] Y. Li, A.M. Wolters, P.V. Malawey, J.V. Sweedler, A.G. Webb, Multiple solenoidal microcoil probes for high-sensitivity, high-throughput nuclear magnetic resonance spectroscopy, Anal. Chem. 71 (1999) 4815–4820.
[18] E. MacNamara, T. Hou, G. Fisher, S. Williams, D. Raftery, Multiplex sample NMR: an approach to high-throughput NMR using a parallel coil probe, Anal. Chim. Acta 397 (1999) 9–16.
[19] T.L. Peck, R.L. Magin, J. Kruse, M. Feng, NMR microspectroscopy using 100 μm planar RF coils fabricated on gallium arsenide substrates, IEEE Trans. Biomed. Eng. 41 (7) (1994) 706–709.
[20] T.L. Peck, J.E. Stocker, Z. Chen, L. LaValle, R.L. Magin, Application of planar microcoils fabricated on glass substrates to NMR microspectroscopy, in: Proceedings of 17th International Conference of the Engineering in Medicine and Biology Society, Montreal, Que., Canada, 20–23 September, 1995, pp. 1547–1548.
[21] J.E. Stocker, T.L. Peck, A.G. Webb, M. Feng, R.L. Magin, Nanoliter volume, high-resolution NMR microspectroscopy using a 60-μm planar microcoil, IEEE Trans. Biomed. Eng. 44 (11) (1997) 1122–1127.
[22] J.D. Trumbull, I.K. Glasgow, D.J. Beebe;, R.L. Magin, Integrating microfabricated fluidic systems and NMR spectroscopy, IEEE Trans. Biomed. Eng. 47 (1) (2000) 3–7.
[23] J. Dechow, A. Forchel, T. Lanz, A. Haase, Fabrication of NMR-microsensors for nanoliter sample volumes, Microelectron. Eng. 53 (2000) 517–519.
[24] C. Massin, G. Boero, F. Vincent, J. Abenhaim, P.-A. Besse, R.S. Popovic, High-Q factor RF planar microcoils for micro-scale NMR spectroscopy, Sensor. Actuat. A 97–98 (2002) 280–288.
[25] C. Massin, A. Daridon, F. Vincent, G. Boero, P.-A. Besse, E. Verpoorte, N.F. de Rooij, R.S. Popovic, A microfabricated probe with integrated coils and channels for on-chip NMR spectroscopy, in: Proceedings of Micro Total Analysis Systems 2001, Kluwer Academic Publishers, Dordrecht, 2001, pp. 438–440.
[26] C. Massin, C. Azevedo, N. Beckmann, P.-A. Besse, R.S. Popovic, Magnetic Resonance Imaging using Microfabricated Planar Coils, in: Proceedings of the IEEE Special Topic Conference on Microtechnologies in Medicine and Biology, 2–4 May 2002 Madison, WI, USA, 2002, pp. 199–204.
[27] D.I. Hoult, R.E. Richards, The signal-to-noise ratio of the nuclear magnetic resonance experiment, J. Magn. Reson. 24 (1976) 71–85.
[28] C.P. Slichter, Principles of Magnetic Resonance, Springer, Heidelberg, 1990.
[29] R.R. Ernst, G. Bodenhausen, A. Waukun, Principles of Nuclear Magnetic Resonance in One and Two Dimensions, Clarendon Press, Oxford, 1987.
[30] F.D. Doty, G. Entzminger, Y.A. Yang, Magnetism in high-resolution NMR probe design. I: General methods, Concepts Magn. Reson. 10 (1998) 133–156.
[31] C.S. Bosch, J.J. Ackerman, Surface coil spectroscopy, NMR Bas. Princ. Prog. 27 (1992) 4–40.
[32] D.I. Hoult, The NMR receiver: a description and analysis of design, Prog. Nucl. Magn. Reson. Spectrosc. 12 (1978) 41–77.
[33] P.T. Callaghan, Principles of Nuclear Magnetic Resonance Microscopy, Clarendon Press, Oxford, 1991.
[34] M.E. Lacey, R. Subramanian, D.L. Olson, A.G. Webb, J.V. Sweedler, High-resolution NMR spectroscopy of sample volumes from 1 nL to 10 μL, Chem. Rev. 99 (1999) 3133–3152.
[35] L.F. Fuks, F.S.C. Huang, C.M. Carter, W.A. Edelstein, P.B. Roemer, Susceptibility, lineshape, and shimming in high-resolution NMR, J. Magn. Reson. B 100 (1992) 229–242.
[36] A.G. Webb, S.C. Grant, Signal-to-noise and magnetic susceptibility trade-offs in solenoidal microcoils for NMR, J. Magn. Reson. B 113 (1996) 83–87.
[37] D. Craik, Magnetism—Principles and Applications, Wiley, Chichester, 1995.
[38] G. Boero, Integrated NMR probe for magnetometry, Ph.D. Thesis, Hartung-Gorre, Konstanz, 2000.
[39] E. Growney, G. Friedman, R. Gerald, Computation of distortions in magnetic field and spectrum for nuclear magnetic resonance instruments, J. Appl. Phys. 85 (1999) 5205–5207.
[40] J. Raz, E.J. Fernandez, J. Gillespie, Modeling NMR lineshapes using logspline density functions, J. Magn. Reson. 127 (1997) 173–183.
[41] A. Homsy, J. Lichtenberg, C. Massin, F. Vincent, P.-A. Besse, R.S. Popovic, N.F. de Rooij, E. Verpoorte, Fabrication of microfluidic channels with symmetric cross-sections for integrated NMR analysis, in: Proceedings of Micro Total Analysis Systems 2002, vol. 1, Kluwer Academic Publishers, Dordrecht, 2002, pp. 115–117.
[42] G.A. Morris, H. Barjat, T.J. Horne, Reference deconvolution methods, Prog. Nucl. Magn. Reson. Spectrosc. 31 (1997) 197–257.
[43] K.R. Metz, M.M. Lam, A.G. Webb, Reference deconvolution: a simple and effective method for resolution enhancement in nuclear magnetic resonance spectroscopy, Concepts Magn. Reson. 12 (2000) 21–42.